Check for updates

Journal of
Materials Chemistry A

Materials for energy and sustainability

rsc.li/materials-a

Volume 6
Number 12
28 March 2018
Pages 4883-5230

ISSN 2050-7488

COMMUNICATION
Zhenhai Wen et al.
An electrochemically neutralized energy-assisted low-cost acid-alkaline electrolyzer for energy-saving electrolysis hydrogen generation

ROYAL SOCIETY
OF CHEMISTRY
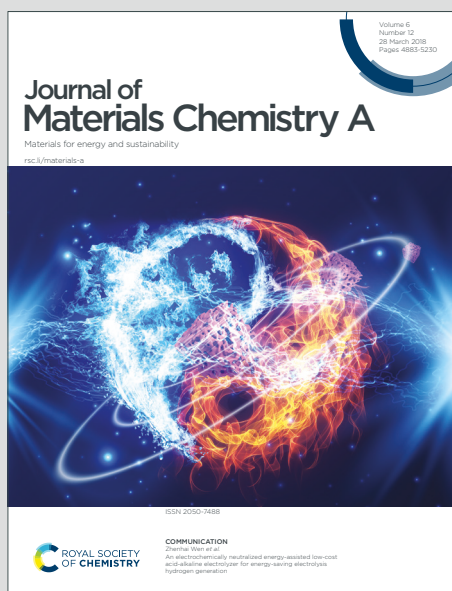
This is an Accepted Manuscript, which has been through the Royal Society of Chemistry peer review process and has been accepted for publication.

Accepted Manuscripts are published online shortly after acceptance, before technical editing, formatting and proof reading. Using this free service, authors can make their results available to the community, in citable form, before we publish the edited article. We will replace this Accepted Manuscript with the edited and formatted Advance Article as soon as it is available.

You can find more information about Accepted Manuscripts in the Information for Authors.

Please note that technical editing may introduce minor changes to the text and/or graphics, which may alter content. The journal's standard Terms & Conditions and the Ethical guidelines still apply. In no event shall the Royal Society of Chemistry be held responsible for any errors or omissions in this Accepted Manuscript or any consequences arising from the use of any information it contains.

ROYAL SOCIETY
OF CHEMISTRY

rsc.li/materials-a

Sustainable Thermoplastic Elastomers-Based Nanocomposites and Their 3D Printing for Flexible and Stretchable Sensors†

Xun Liu,[1] Naifu Shen,[1] Jinyu Bu,[1] Muxuan Yang,[1] Xin Guan,[1] Weinan Xu[1,#,*]

[1] School of Polymer Science and Polymer Engineering, The University of Akron, Akron, OH 44325 USA

ABSTRACT

Stretchable and wearable electronics and devices have brought unprecedented opportunities for many applications including robotics, biomedicine, and artificial intelligence. The fundamental materials that enable such applications generally involve soft conductors that combine conductive nanofillers with soft matrices. However, most current soft conductors rely on conventional soft elastomers such as silicone rubber and polyurethane, which are produced from petrochemicals with limited sustainability. In this study, we developed a series of soft nanocomposites based on the integration of sustainable biobased thermoplastic elastomer polystyrene-*b*-polyfarnesene-*b*-polystyrene (SFS) with carbon nanofillers of different dimensions (2D graphene, 1D carbon nanotube, or 0D carbon black). Importantly, SFS and its nanocomposites are fully compatible with extrusion-based 3D printing. We demonstrated pellet 3D-printing of SFS nanocomposites into functional and customizable 3D structures. The mechanical and electrical properties as well as dynamic responses to mechanical deformation of SFS nanocomposites were systematically investigated for their promising applications in wearable sensors and environment monitoring. We found the type/geometry of carbon nanofillers, the ratio between different types of nanofillers, as well as processing conditions (3D printing vs casting) have significant effects on the electrical properties and strain sensor performance. Such 3D printable soft and sustainable nanocomposites provide a new material platform for applications in soft electronics/robotics and human-machine interfaces.

---

* Corresponding author email: wxu18@utk.edu
# Present Address: Department of Materials Science and Engineering, The University of Tennessee, Knoxville, TN 37996 USA

† Electronic supplementary information (ESI) available: additional characterization of the SFS copolymer and nanocomposites, including GPC, Raman, tensile testing, mechanical and electrical properties data. A detailed description of the analytical modeling of the resistance change as a function of mechanical strain is also included.

Keywords:

Additive manufacturing, polymer nanocomposites, carbon nanomaterials, thermoplastic elastomer, soft electronics

1. Introduction

Stretchable and wearable electronics and sensors are critical components in human-machine interfaces and soft robotics.[1–4] In order to fabricate such soft and stretchable electronics and sensors, one critical component is materials that are stretchable, conductive, and have fast and tunable responses to mechanical deformation.[5,6] The most common method to achieve such properties is by combining a soft elastomer matrix with electrically conductive nanofillers. The commonly used soft matrices for such purposes include silicone elastomers (polydimethylsiloxane),[7,8] polyurethane,[9] natural rubber,[10–12] synthetic rubber[13], thermoplastic elastomers (TPEs)[14] as well as certain types of hydrogels.[15,16] The commonly used conductive nanofillers include metal nanoparticles (NPs),[17,18] nanowires,[19] carbon nanomaterials,[20–23] and liquid metals.[24]

Despite the significant progress and excellent performance achieved for such conventional conductive soft nanocomposites, there are several key issues that need to be addressed. Firstly, most of the current elastomers used as soft matrices are chemically synthesized from petrochemicals, whose sustainability and recyclability are usually very limited.[25] Secondly, the majority of the elastomers and their nanocomposites are not compatible with 3D printing technologies due to their chemically crosslinked structure or unsuitable rheological properties. Thirdly, it is challenging to achieve high sensitivity and stability for both small strains and large strains in the same soft nanocomposite system.[26]

To overcome those limitations, in this study, we develop a new soft and 3D printable nanocomposite system based on biobased sustainable TPEs and their composites with the incorporation of multiple types of carbon nanomaterials. TPE is a category of polymers that combines rubber elasticity with melt processability of thermoplastics.[27,28] This is enabled by their unique molecular structures which contain both a soft elastic/rubbery block and a hard block, the hard blocks act as physical crosslinks to enhance their mechanical strength and stability. One of the most commonly used types of TPEs is styrenic TPEs which have a rubbery soft block and polystyrene hard block, representative examples include polystyrene-b-polyethylene/butylene-b-polystyrene (SEBS), polystyrene-b-polybutadiene-polystyrene (SBS), and poly(styrene-b-isobutylene-b-styrene) (SIBS).[29] However, those conventional styrenic TPEs are based on chemical synthesis with petrochemicals, which have limitations in terms of sustainability and life cycle.

In recent years, biomass-derived materials and monomers have been used for the synthesis of TPEs,[30,31] which provides a new method to enhance the sustainability and carbon emission of TPE production.[32,33] Terpenes, which are naturally abundant and originated from plants are well-suited to this purpose. For instance, one important type of terpenes, β-farnesene, which can be derived from the fermentation of sugar from natural plants, especially sugar cane,[34,35] has been utilized as a biobased monomer to copolymerize with styrene to synthesize new types

of styrenic TPEs.[36,37] Such farnesene-based sustainable TPE will be used as the soft and functional matrix in our study.

Besides the benefits in material sustainability, the use of functional TPEs as the soft matrix for soft electronics/sensors also makes it possible to use 3D printing as a novel method for their fabrication.[38,39] Compared with conventional processing and fabrication such as casting, molding, or extrusion, 3D printing of polymer composites enables customizable and complex 3D geometry fabrication, [40–42]less material waste,[43,44] low tooling cost and reduced lead time[45–47]. The use of 3D printing technologies for the fabrication of soft and wearable sensors is becoming more and more popular, as demonstrated by many recent reports[48,49]. Due to the melt processability of TPEs and their composites, theoretically, they are compatible with extrusion-based 3D printing. However, the most commonly used extrusion-based method, i.e. fused filament fabrication (FFF), is generally not suitable for printing soft elastomers and composites due to issues like filament buckling, poor object/bed adhesion, and unsuitable melt viscosity.[50,51] Direct ink writing (DIW) has also been used to fabricate 3D composite structures with TPE as the soft matrix and showed unique dielectric and optical properties.[52,53] But the DIW method requires the use of organic solvents and rheological modifiers, which are not desirable for many applications.[54,55]

Pellet extrusion-3D printing can potentially overcome those issues and be used for the fabrication of soft electronics/sensors. Compared with the conventional FFF method, pellet-extrusion method can directly use polymer pellets as the feedstock, which are loaded into an extruder that is directly connected to the printing head.[56] Pellet 3D printing also reduces thermal degradation compared to FFF, which helps maintain its structure and physical properties[57,58]. Moreover, it has major advantages of scalability and time and cost saving. It does not require filament fabrication step, which significantly reduces production time and raw materials cost. Although pellet 3D printing exhibits those major advantages, their adoption in the fabrication of soft/stretchable devices using elastomer composites has not been investigated in detail, and this direction holds great potential for further expanding the applications of pellet 3D printing.

In this work, we developed a new sustainable and 3D-printable nanocomposite system that has excellent elasticity, stretchability, tunable internal structures, and strain-dependent electrical properties. Our soft nanocomposites are based on the integration of polystyrene-*b*-polyfarnesene-*b*-polystyrene (SFS) with two types of carbon nanofillers (carbon nanotube and graphene or carbon nanotube and carbon black) with different geometries. Importantly, such soft nanocomposites are fully compatible with pellet 3D printing, which enables the fabrication of customizable and functional structures. The SFS nanocomposites show excellent stretchability (> 1500%), comparable modulus to human skins,[59] and highly tunable electrical conductivity. Their electrical responses to mechanical strain are highly dependent on the nanofiller types and ratio, nanofiller loading, as well as composite processing techniques. Very high gauge factors (GF) of over 3000 can be achieved for strains in the range of 300-500%. We also demonstrate that such SFS nanocomposites can be used for human motion sensing and

environment monitoring with high and consistent performance.

2. Experimental Section

2.1 Materials

SFS polymer (SEPTON BIO SF904) is provided by Kuraray Co., carbon black (BP2000) was purchased from Cabot. Multiwall carbon nanotube was purchased from MSE supplies (Outer Diameter: 10-15 nm, Purity >99%), graphene was purchased from Tianyuan Empire (No. of layer: 1~4 (≥95%)). Toluene and other solvents were purchased from Fisher Scientific. All chemicals were used as received without further purification.

2.2 SFS nanocomposites and pellets preparation

The carbon nanomaterials (CNT and CB, or CNT and Graphene) were mixed in a predetermined ratio and then dispersed in toluene. The solution was bath sonicated for 1 hour to achieve homogeneous dispersion of the nanofillers. Then a corresponding amount of SFS polymer was added to the solution and stirred until the polymer was completely dissolved. The composite solution was then cast into a glass petri dish and the solvent was evaporated to form a solid composite membrane. The composite membrane was then cut into small pieces (4x4 mm) with scissors and used as the feeding stock for pellet 3D printing.

2.3 Pellet extrusion 3D printing

SFS or its composite pellets were loaded into the hopper of a desktop pellet-extrusion 3D printer (Tumaker NX Pro). The printer is equipped with two vertically aligned miniature screw extruders for extruding granules. Two independent heating zones in each extruder provide accurate temperature control. The screw has a diameter of 8 mm, an L/D ratio of 7.5, and a compression ratio of 1.7:1. The printing nozzle diameter is 800 μm. The printing temperature was set at 175 °C for pristine SFS, and 205 °C for SFS nanocomposites. The build plate temperature was set at 80 °C. The layer height was set at 0.2 mm. The printing speed can be varied from 4 to 20 mm/s. The printing head moves in the x and y directions controlled by the digital model while the build plate moves in the z direction. The 3D models were built using SolidWorks and the slicing was done with SuperSlicer.

2.4 Characterization

Scanning electron microscopy (SEM) was conducted using a JEOL-7401 FE-SEM at 5 kV accelerating voltage. Fourier transform infrared (FTIR) spectra were collected (Nicolet iS50, Thermo Scientific) in attenuated total reflection mode. The data were an accumulation of 128 scans at a resolution of 4 cm^{-1} in the range of 4000–400 cm^{-1}. GPC experiments were carried out using Tosoh EcoSEC HLC-8320 with THF as the solvent at a flow rate of 1 mL/min and

40 °C. Thermal stability was studied by thermogravimetric analysis (TGA) (TA Q50). The temperature range was from room temperature to 600 °C at a heating rate of 10 °C min^{-1}. The experiment was conducted under a nitrogen atmosphere. Hardness was determined with a Shore A Digital hardness tester according to ISO 868-1986. Raman spectra were collected with a Renishaw inVia confocal Raman microscope with an excitation wavelength of 514 nm. Differential scanning calorimetry (DSC) was performed on TA Instruments Q200 with aluminum hermetic pans. Tensile tests were conducted with an Instron 5567 Tensile Tester according to the ISO 37 standard procedure. The electrical properties of the nanocomposites and strain sensor performance were measured using a Keithley 2400 source meter. The programmed or cyclic stretching and relaxing were done with a custom-built automated biaxial stage with AC brushless servo motors (Parker Hannifin SM231AL-NPSN).

3. Results and Discussion

3.1 Structure and properties of sustainable SFS elastomer

The TPE used in our study is a triblock copolymer composed of biobased monomer β-farnesene and styrene. Its synthesis and chemical structure are shown in Figure 1a. The two blocks at both ends are polystyrene, and the middle block is polyfarnesene, so it is named SFS in this manuscript (S stands for polystyrene, and F stands for polyfarnesene. The hard polystyrene blocks act as physical crosslinks to enhance the mechanical strength and stability of the SFS. The molar mass of SFS (Mn = 54.0 kDa, Đ = 1.24, see Figure S1) was determined using GPC. The weight fraction of the polystyrene block of SFS in our study is 21%, and the elastomer has a hardness of 25 Shore A. The main role of the polystyrene (PS) block is to enhance the mechanical strength, while maintaining the melt processability of the resulting copolymer. The middle polyfarnesene block is hydrogenated to enhance the thermal and chemical stability of the SFS copolymers. From the chemical structure of SFS, it can be seen that the β-farnesene repeating unit forms short branches from the backbone, such unique bottlebrush-like structure in the soft middle block further contributes to the softness and flexibility of SFS.
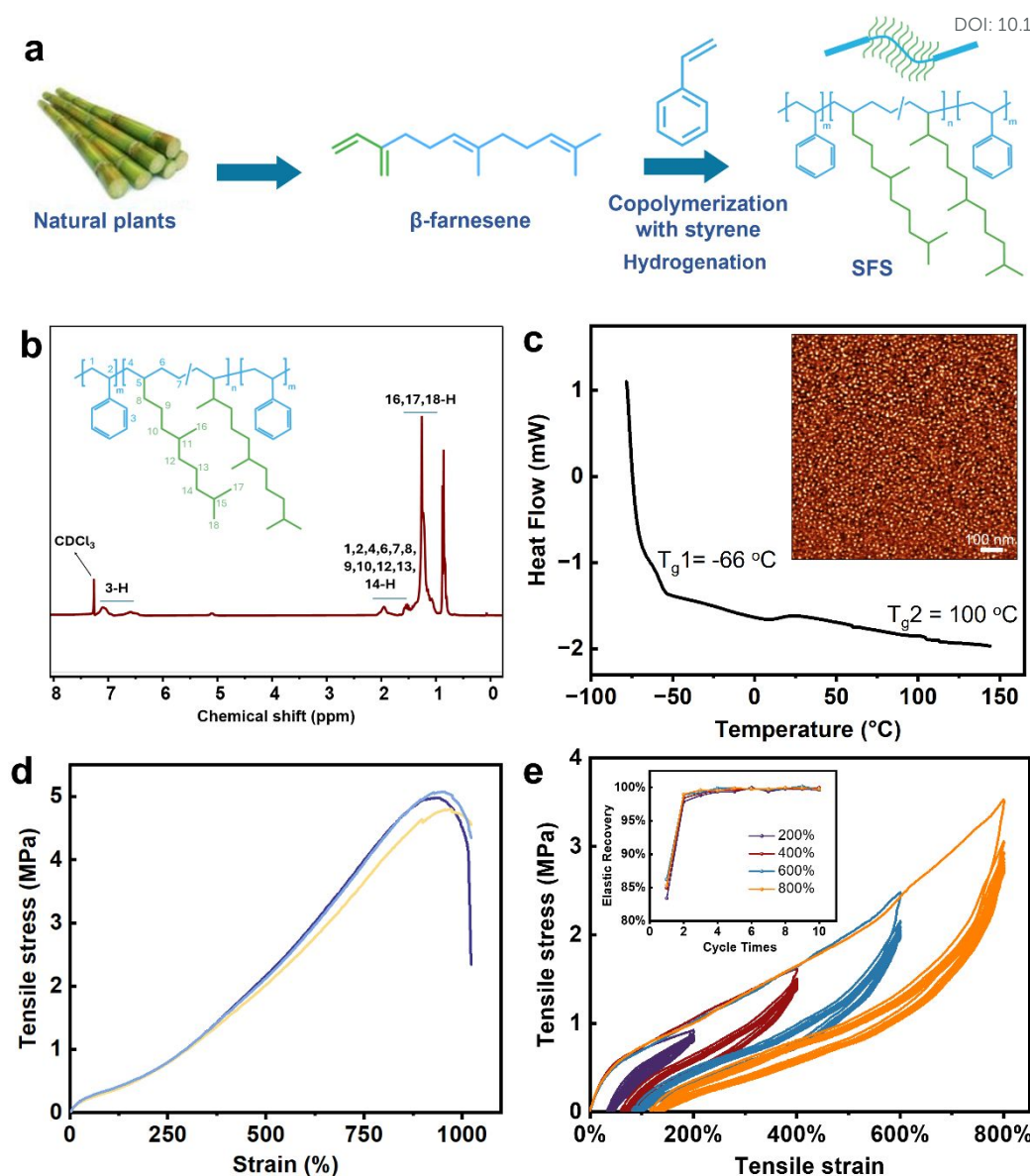
Figure 1. (a) Schematic of the synthesis and chemical structure of SFS elastomer. (b) ^{1}H NMR spectrum of SFS. (c) DSC of SFS shows two glass transitions of the hard and soft blocks. Inset shows the AFM phase image of a SFS thin film. (d) Representative tensile stress-strain curves of SFS. (e) Cycling tests of SFS with a maximum strain of 200%, 400%, 600%, and 800% at a rate of 200 mm/min, ten cycles of testing at each maximum strain are shown. Inset shows the elastic recovery ratio of SFS during the cyclic tests with different maximum strains.

We systematically characterized the structure and properties of SFS. The ^{1}H NMR spectrum confirms the chemical structures of SFS with the corresponding locations labeled (Figure 1b). The DSC data (Figure 1c) shows two glass transition temperatures, the one at -66 °C corresponds to the glass transition of polyfarnesene block and the one at 100 °C corresponds to the glass transition of polystyrene block. The broad exothermic peak at about 35 °C is attributed to the twisting and alignment of the aromatic centers along an ordered axis of the polystyrene block[60]. AFM characterization of SFS (Figure 1c inset) shows well-defined

microphase-separated morphology between the polystyrene and polyfarnesene blocks. The bright spherical domains correspond to PS and the dark matrix corresponds to the polyfarnesene domain.

One of the most important features for choosing SFS as the polymer matrix for the fabrication and 3D printing of soft sensors is its mechanical properties. The representative tensile stress-strain curves of SFS (samples prepared by compression molding at 165 °C for 60 mins.) are shown in Figure 1d. The SFS shows an average tensile strength of 5.0 MPa, elongation at break of 1030%, Young's modulus of 0.9 MPa, and M100 modulus (strength at 100% elongation) of 0.35 MPa. The SFS material exhibits a relatively low modulus, making it highly suitable for use as soft and wearable sensors and devices that require excellent compliance and comfort when in contact with the human body. Such mechanical properties are better (especially higher elongation at break) or comparable with other commonly used soft materials for flexible sensors and electronics including PDMS and polyurethane.[7,61]

Cyclic tensile testing with different maximum strains was also conducted on SFS (Figure 1e), it can be seen that after the first loading-unloading cycle, the 2nd loading shows an obvious softening or decrease in modulus, and then the following cycles closely match each other. This can be explained by the classic Mullins effect.[61–63] During the first stretching, there is some extent of disentanglement of polymer chains and physical crosslinking, as well as slippage of molecular chains, so that hysteresis under cyclic loading and strain-softening occur.[64] The elastic recovery ratio of SFS during the cyclic tests is shown in Figure 1e inset, which further shows that after the first loading cycle, the SFS maintains stable and fully reversible (> 99% recovery) against mechanical deformation, which is beneficial for its application in flexible electronics and sensors.

3.2 Pellet 3D Printing of SFS Elastomer

The SFS elastomer and its nanocomposites are compatible with extrusion-based 3D printing because they are not chemically crosslinked. The most commonly used method for extrusion-based 3D printing is fused filament fabrication (FFF), which involves the melting and extrusion of a plastic filament from a heated nozzle on the platform in a layer-by-layer manner. However, FFF is not suitable for printing soft elastomers because soft filaments cannot be consistently and continuously extruded without buckling. Moreover, the filament fabrication process adds additional cost and time to the process. In this study, we overcome this issue by using pellet 3D printing for SFS and its composites. In comparison with FFF, pellet 3D printing (Figure 2a) can use polymer pellets directly without the need for filament fabrication, which reduces production time and raw materials cost. Moreover, it enables a broader selection of materials, soft TPEs such as SFS are fully compatible with the printing process.
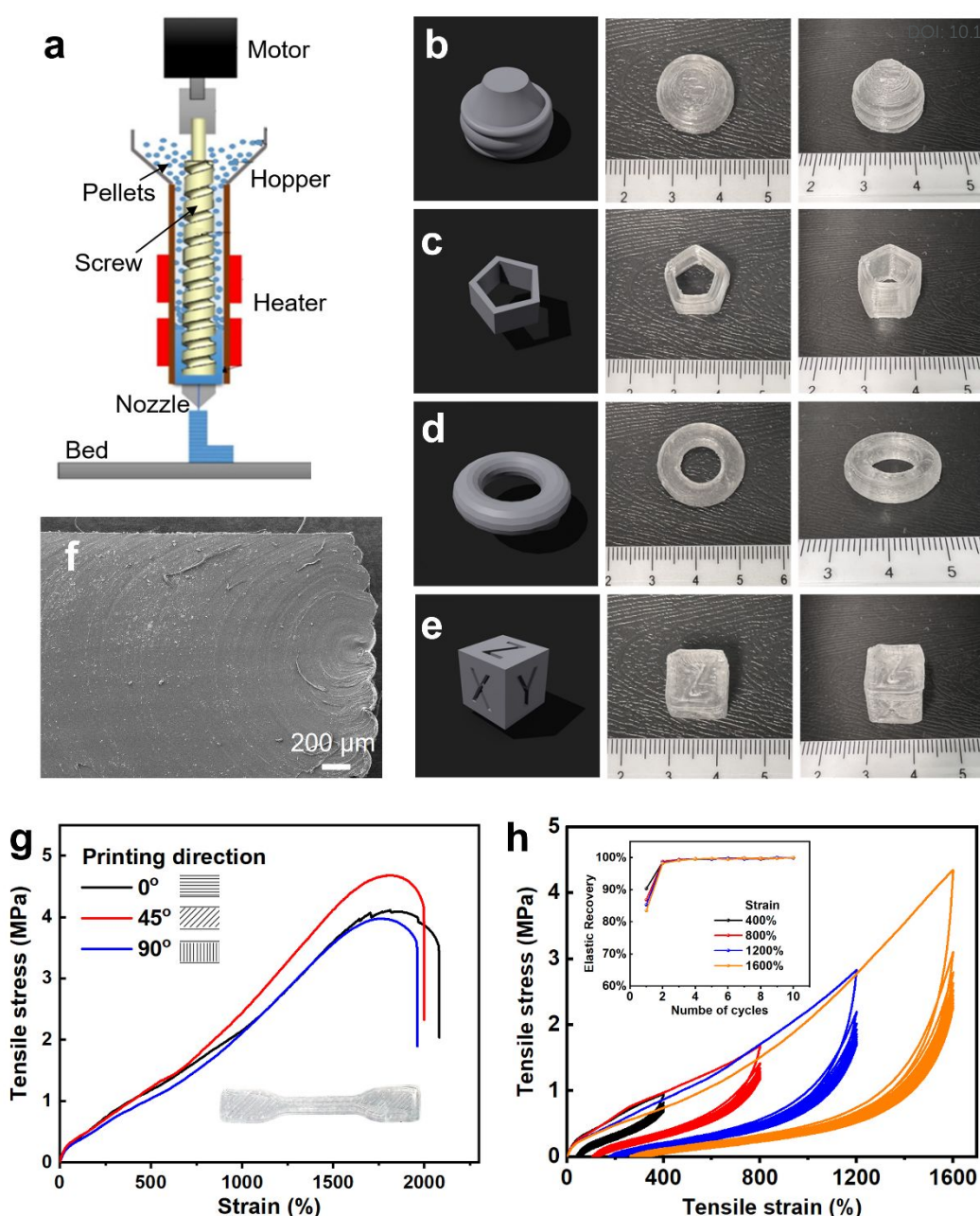
Figure 2. (a) Schematic of pellet-extrusion 3D printing. (b-e) Representative 3D structures printed from SFS pellets, including (b) inverted bowl, (c) pentagon prism, (d) circular tube, and (e) cubic dice. The first column is the 3D model, the second column is the top view, and the third column is the tilted view. (f) Cross-section SEM of the 3D-printed SFS structure. (g) Representative stress-strain curves of pellet 3D-printed SFS with different printing directions. The inset shows the photo of a typical 3D-printed dogbone with 45° printing direction. (h) Cycling tests of 3D-printed SFS with a maximum strain of 400%, 800%, 1200%, and 1600% at a rate of 200 mm/min, ten cycles of testing at each maximum strain are shown. Inset shows the elastic recovery ratio of SFS during the cyclic tests with different maximum strains.

The main parameters that need to be controlled and optimized during pellet 3D printing of SFS include loading chamber temperature (inside the single screw extruder), nozzle temperature, and printing bed temperature, which is set at 150 °C, 175 °C, and 80 °C,

respectively. The nozzle diameter is 0.8 mm and layer height is set at 0.2 mm. Those parameters are determined after varying them in a range and optimization based on the final printing quality. Representative 3D structures with different geometries such as inverted bowl and pentagon prism are shown in Figure 2b-e. High printing quality and shape fidelity are achieved, and the difference between actual dimensions and the corresponding digital model is within 3%. The pellet 3D-printed structures also have dense and solid internal structure, as shown by the cross-section SEM image in Figure 2f. The surface and edge of the printed structure still shows layered morphology that is typical for extrusion-based 3D printing (Figure S2).

We also studied the mechanical properties of SFS structures fabricated by pellet 3D printing (printing temperature of 175 °C). It is known that the mechanical properties of 3D structures by extrusion-based 3D printing generally depend on the printing direction. For instance, for the pellet 3D-printed dogbone samples, printing direction of 0°, 90°, or 45° means the traveling path of the printing nozzle is parallel, perpendicular, or has a 45° angle in reference to the long axis of the dogbone. Tensile testing of the samples printed with those three directions shows very similar mechanical properties (Figure 2g). For instance, The average tensile strength is 4.69, 4.63, and 4.11 MPa for samples with printing directions of 0°, 45°, and 90°, respectively. The average Young's modulus for the samples with printing direction of 0°, 45°, and 90°, are 1.10, 0.89, and 0.89 MPa, respectively. Those values are also very close to SFS structures made by compression molding.

Interestingly, the elongation at break for the pellet 3D-printed samples is about 2000%, which is much higher than that of compression-molded SFS (about 1000%, Figure 1d). The main reason for such a difference is probably that during pellet 3D printing, SFS chains are thermally processed in the extruder for a longer time compared with compression molding, such thermal annealing effect leads to a denser and better-ordered internal structure. Cyclic tensile testing with different maximum strains was also conducted on pellet 3D-printed SFS (Figure 2h, see also Figure S3). Obvious hysteresis and strain-softening occur during the first stretching, and then the structure becomes stable and fully recoverable during subsequent mechanical deformation with an elastic recovery ratio over 99%.

3.3 SFS nanocomposites preparation and their morphologies

In order to make soft and conductive structures and devices with SFS as the matrix, we incorporated carbon nanomaterials as nanofillers into SFS. The commonly used carbon nanomaterials as conductive fillers include graphene, multiwall carbon nanotube (CNT), and carbon black (CB), which belong to 2D, 1D, and 0D nanomaterials, respectively. We initially tested with only graphene as the nanofiller, but the conductivity of SFS-graphene composites is relatively low (10^{-5} S/m) even with the incorporation of 10 wt.% graphene (Figure S4). In order to achieve higher electrical conductivity and sensitivity, in this study we focused on combining two types of carbon nanomaterials (CNT and graphene, or CNT and CB) into SFS
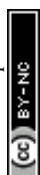
matrix to create flexible and conductive nanocomposites. The integration of two types of nanofillers also enables a wider range of electrical properties and strain responses of the nanocomposites, as shown in the next section. Besides enhancing the physical properties, the combination of two types of carbon nanofillers also has the benefits of decreasing the overall cost of such nanocomposites, because CB has a much lower price than that of graphene or CNT.[65,66]
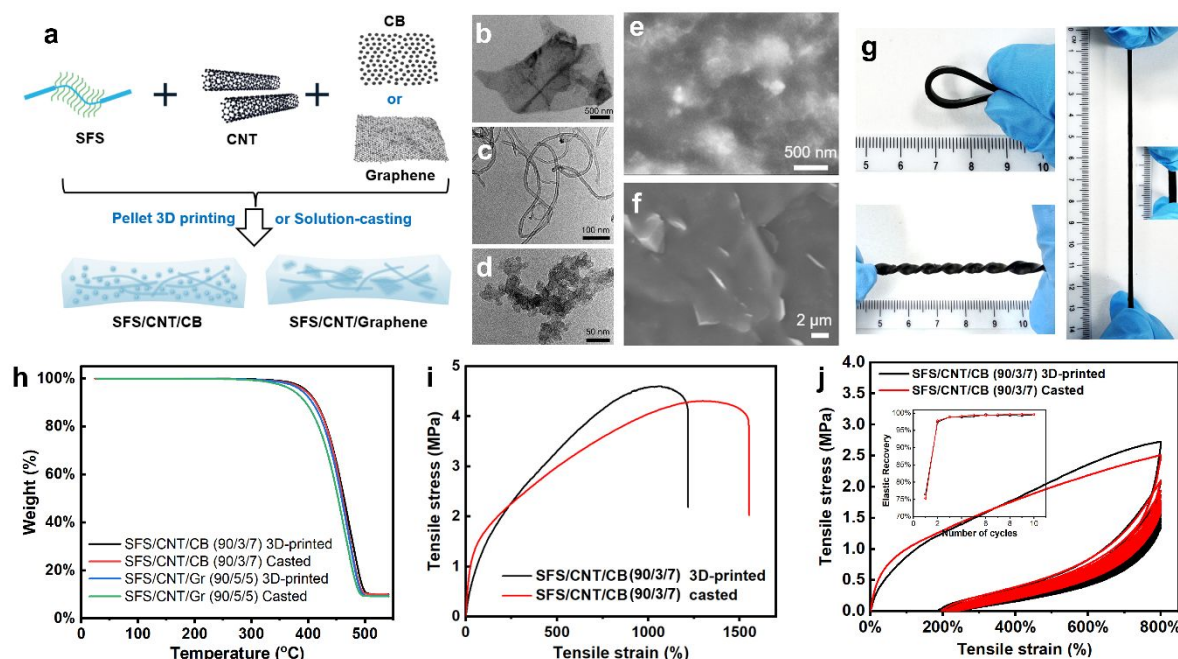

Figure 3. (a) Schematic of the SFS-based nanocomposites fabrication process. (b-d) TEM images of the graphene (b), CNT (c), and carbon black (d). (e-f) Cross-section SEM images of SFS/CNT/CB (90/3/7) (e) and SFS/CNT/Gr (90/5/5) (f) nanocomposites. (g) Demonstration of the mechanical flexibility and stretchability of SFS/CNT/CB (90/3/7) nanocomposite. (h) TGA curves for the different types of SFS-based nanocomposites fabricated by pellet 3D printing or solution casting. (i) Representative tensile stress-strain curves for SFS/CNT/CB (90/3/7) fabricated by pellet 3D printing and solution casting. (j) Cycling tests of SFS/CNT/CB (90/3/7) with maximum strain of 800%, ten testing cycles at the maximum strain are shown. The inset shows the elastic recovery ratio of SFS/CNT/CB (90/3/7) during the cyclic test.

The carbon nanomaterials were mixed with SFS by solution blending and then the nanocomposites can be prepared by two different methods: solution casting or pellet 3D printing (Figure 3a). We focus on two types of nanocomposites with different combinations of carbon nanofillers: SFS/CNT/CB represents SFS composites with CNT and CB incorporated, SFS/CNT/Gr represents SFS composites with CNT and graphene incorporated, the weight ratio between those components is indicated by the number in the bracket after the name such as SFS/CNT/CB (90/3/7). TEM images of the three types of carbon nanomaterials (Figure 3b-d) confirm their morphologies and dimensions. The lateral size of graphene is from hundreds of

nm to several μm; the diameter of CNT is about 10 nm; the average size of CB is about 20-30 nm.

The internal structures of the nanocomposites were studied by cross-section SEM (Figure 3e-f). The SFS/CNT/CB composite shows a high density of fiber-like CNTs and CB NPs, which have a relatively good dispersion in the SFS matrix, and the CB NPs can form local aggregates. On the other hand, the SFS/CNT/Gr (90/5/5) composite shows quite different morphology with 2D graphene nanoflakes clearly visible. The total weight percentage of the carbon nanofillers in the composites is kept at 10 wt%, this is confirmed by the TGA analysis (Figure 3h), which shows the residual weight at 500 °C is very close to 10%. The ratio between the two types of nanofillers (CNT:CB or CNT:Gr) was also varied and optimized based on the electrical resistance and sensitivity achieved in the nanocomposites, as will be discussed in the next section. The two types of nanocomposites we will focus on are SFS/CNT/CB (90/3/7) and SFS/CNT/Gr (90/5/5). Raman spectra of those carbon nanomaterials as well as the SFS nanocomposites show the characteristic peaks of graphene, CNT and CB. (Figure S5).

The SFS-based nanocomposites are still highly flexible and stretchable, as shown by the bending, twisting, and stretching demonstrations in Figure 3g. The mechanical properties of the nanocomposites fabricated by both solution casting and pellet 3D printing (printing temperature of 205 °C) were studied and compared. The representative tensile stress-strain curves for SFS/CNT/CB (90/3/7) nanocomposites are shown in Figure 3i. Compared with pristine SFS (Figure 1d), the SFS nanocomposites show higher modulus and higher elongation at break due to the reinforcement of the carbon nanofillers. For instance, the SFS/CNT/CB (90/3/7) fabricated by solution casting shows Young's modulus of 44.9 MPa, M100 modulus of 1.68 MPa, and elongation at break of 1550%.

Moreover, the fabrication method also has substantial effects on the mechanical properties of SFS nanocomposites. The SFS/CNT/CB (90/3/7) fabricated by solution casting shows similar tensile strength (4.3 MPa vs 4.6 MPa), higher modulus (1.68 MPa vs 1.38 MPa M100 modulus) and higher elongation at break (1550% vs 1220%) compared with the samples prepared by pellet 3D printing. Cyclic tensile testing on SFS/CNT/CB (90/3/7) fabricated by both solution casting and pellet 3D printing was conducted (Figure 3j). It can be seen that they show almost identical properties, with obvious hysteresis during the first stretching cycle, and then maintain highly stable and reversible elastic recovery (> 98%).

3.4 Electrical properties and strain response of the SFS nanocomposites

We studied the electrical conductivity and its responses to mechanical strain of the SFS nanocomposites. The findings are very interesting and show that the types of nanofillers, their morphologies and ratios, as well as the mechanical deformation rate, all have significant effects on the electrical properties. Three types of SFS nanocomposites were investigated and compared: SFS/CNT/Gr (90/5/5), SFS/CNT/CB (90/5/5), and SFS/CNT/CB (90/3/7). A comparative study of the first two types will show the effect of nanofiller

dimension/morphology, and comparative study of the latter two types will show the effect of ratios between the nanofillers. The total weight fraction of the carbon nanofillers is fixed at 10% because at lower fractions the electrical conductivity is substantially lower. For instance, the electrical resistance of SFS/CNT/Gr (95/2.5/2.5) is about 500 times higher than that of SFS/CNT/Gr (90/5/5) (Figure S6).
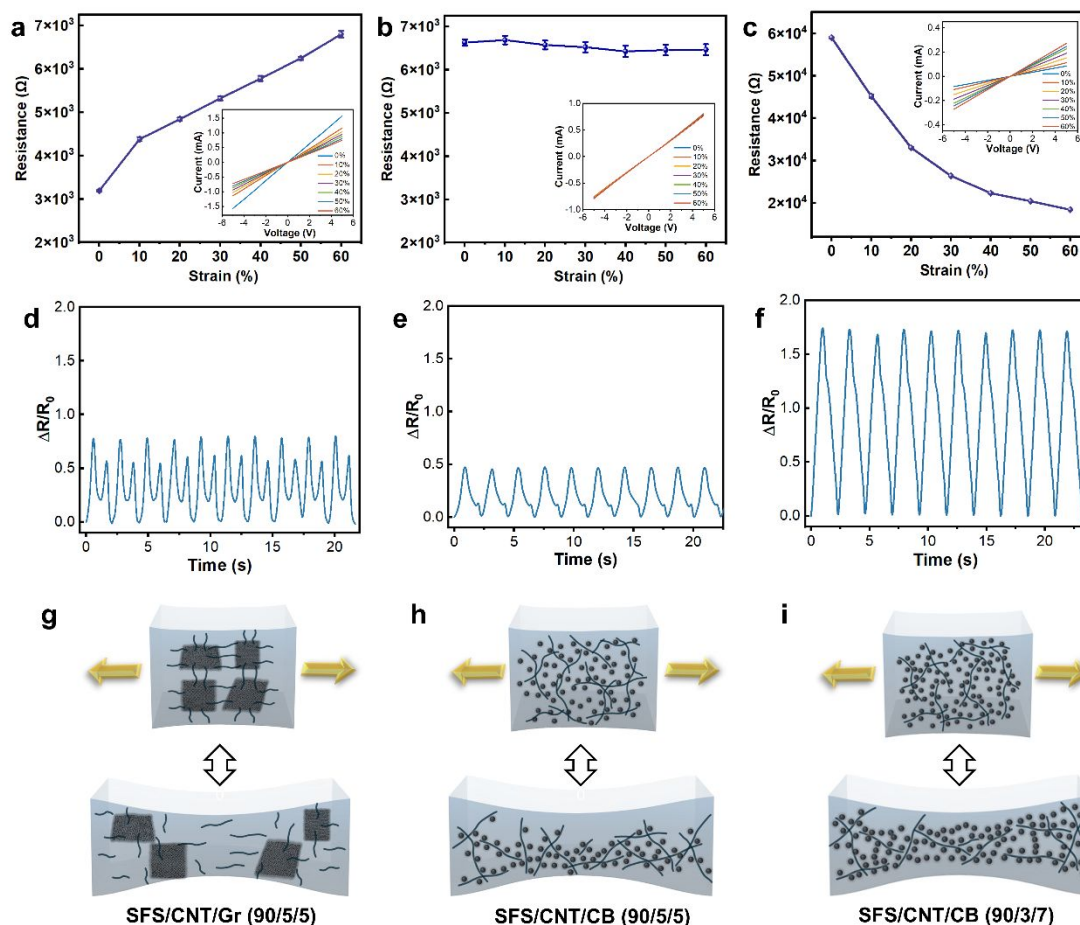

Figure 4. (a-c) Resistance change as a function of tensile strain for (a) SFS/CNT/Gr (90/5/5), (b) SFS/CNT/CB (90/5/5), and (c) SFS/CNT/CB (90/3/7). Note panel c has a different Y scale. Inset in each panel is the corresponding I-V curves. (d-f) Relative resistance change ($\Delta R/R_0$) as a function of time during the cyclic deformation of (d) SFS/CNT/Gr (90/5/5), (e) SFS/CNT/CB (90/5/5), and (f) SFS/CNT/CB (90/3/7). The cyclic testing was conducted at a frequency of 0.45 Hz and a maximum strain of 50%. (g-i) Schematic of the proposed internal structural changes during mechanical deformation of the three types of SFS nanocomposites.

In the relaxed state with 0% strain, SFS/CNT/Gr (90/5/5) nanocomposite shows a resistance of about 3.2 kΩ. With the increase of stretching strain, it shows a near linear increase in resistance (Figure 4a), for instance, the resistance increases to 6.8 kΩ at 60% strain. Note that such resistance vs strain data is obtained at the structural equilibrium state (after resistance reaches a stable value, usually about 3 minutes) in each strain. The corresponding I-V curves

at different strains are also shown (Figure 4a inset). In contrast, when 2D graphene is replaced with 0D carbon black, the SFS/CNT/CB (90/5/5) nanocomposite shows quite stable electrical resistance against strain (Figure 4b). For instance, the resistance values at 0% and 60% strain are very close to each other at 6.6 kΩ and 6.5 kΩ, respectively. Moreover, when the ratio between CNT and CB changes to 3:7, the SFS/CNT/CB (90/3/7) nanocomposite shows a substantial decrease in electrical resistance with increasing strain (Figure 4c). For instance, its resistance decreases from 59 kΩ at 0% strain to 18 kΩ at 60% strain, which is different from both of the previous two types of nanocomposites. It is noted that the resistivity-strain relationship would follow the same trends due to the standardized sample dimensions.

The dynamic responses of electrical resistance against mechanical strain are also quite different for the three types of SFS nanocomposites. The relative resistance change ($\Delta R/R_0$, absolute value) as a function of time during cyclic deformation of SFS/CNT/Gr (90/5/5) is shown in Figure 4d. The resistance response in each stretching-relaxation cycle is not the typical monotonic increase till maximum strain and then decrease to the original value, instead, it shows a peak value during the stretching, and another smaller peak value during the relaxation step. Such double-peak response of SFS/CNT/Gr (90/5/5) persists despite varying the maximum strain or cyclic loading frequencies (Figure S7 and S8).

When graphene is replaced by carbon black, the SFS/CNT/CB (90/5/5) nanocomposite shows a different dynamic response (Figure 4e), which still has two peaks during each stretching-relaxation cycle, but the peak during stretching is much more dominant. On the other hand, the SFS/CNT/CB (90/3/7) nanocomposite (Figure 4f) shows a more typical dynamic response with an almost linear decrease in resistance till maximum strain followed by a linear increase during the relaxation step.

Such interesting and highly tunable electrical properties responses can be explained by the differences in their internal structure, especially the conductive network formation and disruption during mechanical deformation. For the SFS/CNT/Gr (90/5/5) nanocomposite, the conductive pathways are formed by 1D CNT bridging the 2D graphene nanosheets (Figure 4g). When the composite is under stretching, it is easy for such connections between CNT and graphene to break, thus, decreasing the number of conductive pathways and resulting in resistance increase.

For SFS/CNT/CB (90/5/5) nanocomposite, the amount/density of 1D CNT and 0D CB is similar, they also have a strong affinity to each other. Therefore, in the relaxed state, the conductive pathways are formed mostly by the interconnected network of curved CNT with CB particles mostly located along the CNT network (Figure 4h). Upon mechanical stretching (small to medium stain, before network disruption), the curved CNT gets straightened and better aligned along the stretching direction, and most of the junctions are maintained. That's why the conductivity is largely maintained despite the increase in strain.

On the other hand, for the SFS/CNT/CB (90/3/7) nanocomposite, CB is the majority nanofiller, so in the relaxed state, besides the conductive pathways formed by CNT and CB, there are also excess CB nanoparticles dispersed in SFS matrix without forming effective conductive channels (Figure 4i). When mechanical stretching is applied, the excess CB nanoparticles can form additional conductive pathways due to the alignment and decreased interparticle distance. Therefore, the electrical resistance for SFS/CNT/CB (90/3/7) nanocomposite decreases with increasing strain.

To explain the unusual double-peak responses of SFS/CNT/Gr nanocomposites when subjected to cyclic mechanical strains, we conducted additional experiments by fixing the amount of SFS and CNT and varied the content of graphene in the three composites: SFS/CNT/Gr (90/5/2.5), SFS/CNT/Gr (90/5/5), and SFS/CNT/Gr (90/5/10). The resistance changes as a function of tensile strain and dynamic responses against cyclic strain are shown in Figure S9 and S10. When the graphene content is low, namely SFS/CNT/Gr (90/5/2.5), the electrical response is very close to conventional monotonic increase and then decreases to the original value. While for the two samples with higher graphene content, they show double-peak behavior.

Such comparative study shows that the double-peak behavior is primarily due to the existence of 2D graphene, especially when it acts as the main conductive nanofiller. Due to its ultrathin structure and low bending stiffness, a fraction of graphene nanosheets are wrinkled or partially folded in the relaxed state (Figure. 3b). During the stretching cycle, with the increase in strain, those graphene nanosheets first flatten and increase the effective volume fraction of conductive nanofillers, which leads to decrease in resistance. Then with further increasing in strain, the separation or distance between the conductive nanofillers increases, which leads to an increase in resistance. The reverse process occurs during the relaxation cycle.

3.5 Electrical properties and strain response of 3D-printed SFS nanocomposites

Pellet 3D printing was used as a novel method for fabricating soft and conductive SFS nanocomposites. We found that nanocomposites fabricated by pellet 3D printing show substantially different electrical properties and dynamic responses compared with those fabricated by solution casting. The internal structure of pellet 3D-printed SFS/CNT/CB (90/3/7) nanocomposite (Figure 5a) is studied by cross-section SEM. The printed nanocomposites have a dense internal structure (Figure 5b) without visible gaps or holes. Higher magnification SEM image shows fiber-like CNTs and CB NPs uniformly distributed in the polymer matrix. Moreover, the CNTs have a certain degree of preferential alignment along the printing direction marked by the yellow arrow (Figure 5c).
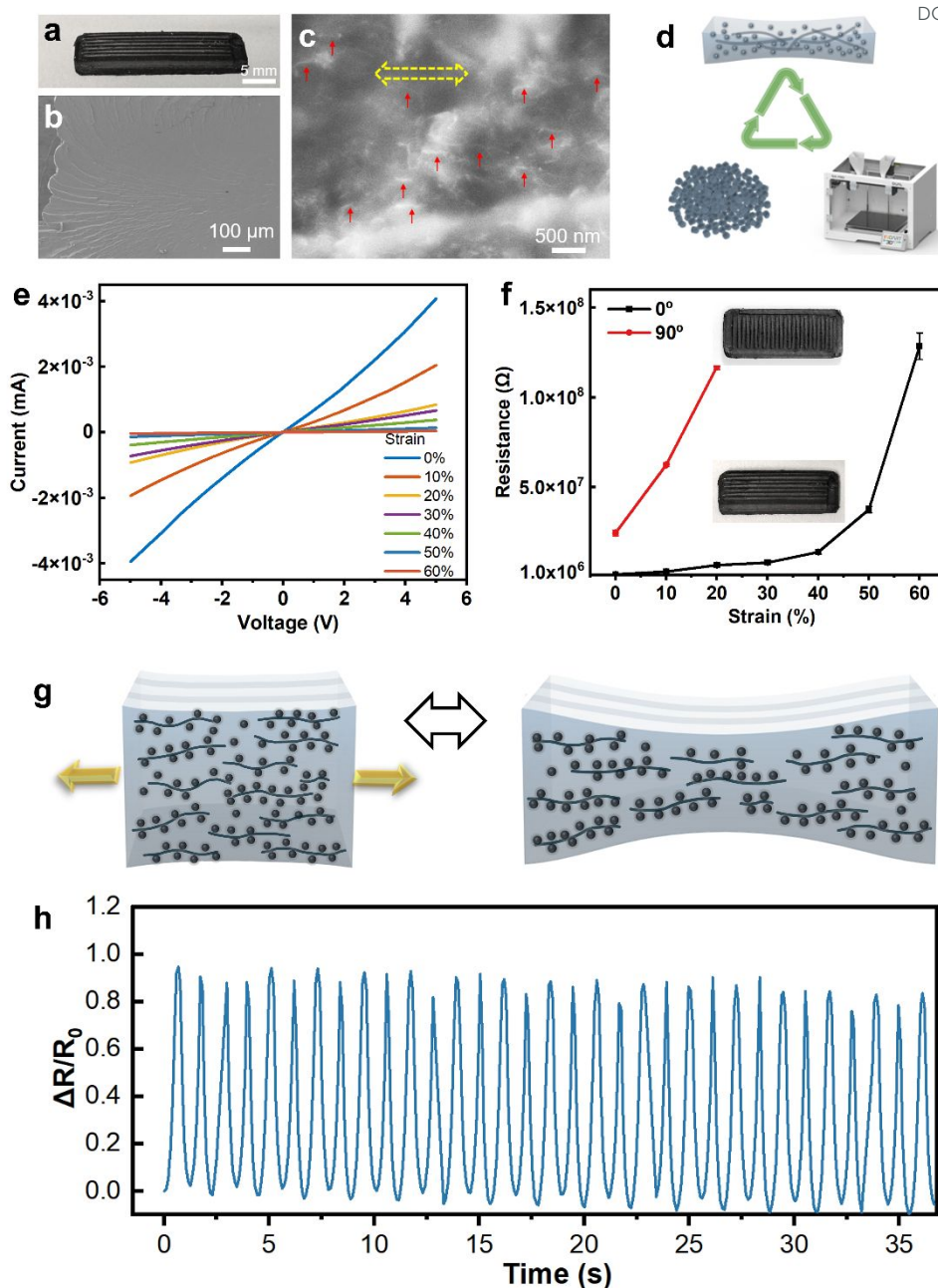
Figure 5. (a) Photo of a pellet 3D-printed SFS/CNT/CB (90/3/7) nanocomposite with a rectangle shape. (b-c) Cross-section SEM images of the 3D-printed SFS/CNT/CB (90/3/7) at two different magnifications. Red arrows in (c) show representative locations where CNTs are aligned. (d) Schematic of recyclability of the SFS nanocomposites by pelletization and repeated 3D printing. (e) I-V curves of the 3D-printed SFS/CNT/CB (90/3/7) at different equilibrium strains. (f) Resistance changes as a function of equilibrium strains for the 3D-printed SFS/CNT/CB (90/3/7). The black curve corresponds to the sample printed along the long axis (0°), and the red curve corresponds to the sample printed along the short axis (90°). (g) Schematic of the internal structural changes of 3D-printed SFS/CNT/CB during mechanical stretching. (h) Relative resistance change ($\Delta R/R_0$) of 3D-printed SFS/CNT/CB (90/3/7) nanocomposite (printing direction of 0°) under cyclic stretching at 30% maximum strain under a frequency of 0.9 Hz.

Another advantage of our SFS nanocomposites is that they can be physically recycled and used for multiple cycles. Because there is no chemical crosslinking, our SFS nanocomposites can be reprocessed for new printing or recovery of polymers and nanofillers for new applications. For instance, the 3D-printed nanocomposite structures can be pelletized into composite pellets and then used as the starting raw material for new pellet 3D printing (Figure 5d). This is demonstrated with the pellet-printed SFS/CNT/CB (90/3/7) nanocomposites (Figure S11), the recycled and reprinted structures have comparable morphology and mechanical properties compared with the original ones.

The unique internal structure leads to very different electrical properties of the pellet 3D-printed SFS/CNT/CB (90/3/7) (Figure 5e-f). The sample shows a significant increase in electrical resistance from $1.1 \times 10^6\ \Omega$ to $1.2 \times 10^8\ \Omega$ when the mechanical strain increases from 0% to 60%, in contrast to the decreasing trend of resistance for the solution-cased sample with the same composition. The probable reason for such a drastic difference is schematically shown in Figure 5g. Due to the shear force in the extruder and printing nozzle during pellet 3D printing, there will be preferential orientation of stretched CNTs along the printing direction. A fraction of CB nanoparticles are located adjacent to CNTs, and the rest are dispersed in the SFS matrix. In the relaxed state, the junctions between the aligned CNTs are the primary pathways for electric conduction. Upon mechanical stretching, the stretched CNTs are easily separated from one another, and the density of conductive pathways is substantially reduced, which leads to an increase in electric resistance.

Moreover, the shear-induced alignment especially on the CNT component during pellet 3D printing also leads to anisotropic electrical properties. To demonstrate this, we printed SFS/CNT/CB (90/3/7) nanocomposites into the same rectangle shape but with different printing directions: parallel to the long axis ($0°$) and perpendicular to the long axis ($90°$) (Figure 5f). The electrical conductivity along the long axis is much higher for the $0°$ sample than that of the $90°$ sample (resistance at relaxed state: $1.1 \times 10^6\ \Omega$ vs $2.5 \times 10^7\ \Omega$). Such differences in electrical conductivity get more pronounced when the sample is stretched along the long axis. In addition, the dynamic response of 3D-printed SFS/CNT/CB (90/3/7) upon cyclic stretching is still fast and consistent over long cycles (Figure 5h).

To summarize the major differences in properties of the 3D-printed and solution-cast SFS nanocomposites, we observed that the 3D-printed samples have comparable mechanical properties with the solution-casted ones, while the electrical responses are dramatically different due to the nanofiller dispersion and alignment. At the same composition, the 3D-printed nanocomposites show lower electrical conductivity but more pronounced changes in response to mechanical strain, which can be further tuned by controlling the printing direction.

3.6 Systematic study of SFS nanocomposites-based strain sensors

From the comparative study of multiple types of SFS nanocomposites as well as the fabrication approaches, it can be seen that SFS/CNT/CB (90/3/7) nanocomposite from solution

casting has the highest response sensitivity upon dynamic mechanical loading, and therefore
its strain sensor performance is more systematically study, as discussed below. The electrical
response of SFS/CNT/CB (90/3/7) against cyclic stretching with different maximum strain is
shown in Figure 6a. The relative resistance change is stable and consistent at all the different
stain conditions. The peak value of $\Delta R/R_0$ also increases from 0.9 at 20% maximum strain to
2.8 at 80% maximum strain. The dynamic response of SFS/CNT/CB (90/3/7) nanocomposite
to applied strain (40% maximum) with varying frequencies from 0.125 to 0.4 Hz is shown in
Figure 6b (additional data are in Figure S12). The responses are rapid and match with
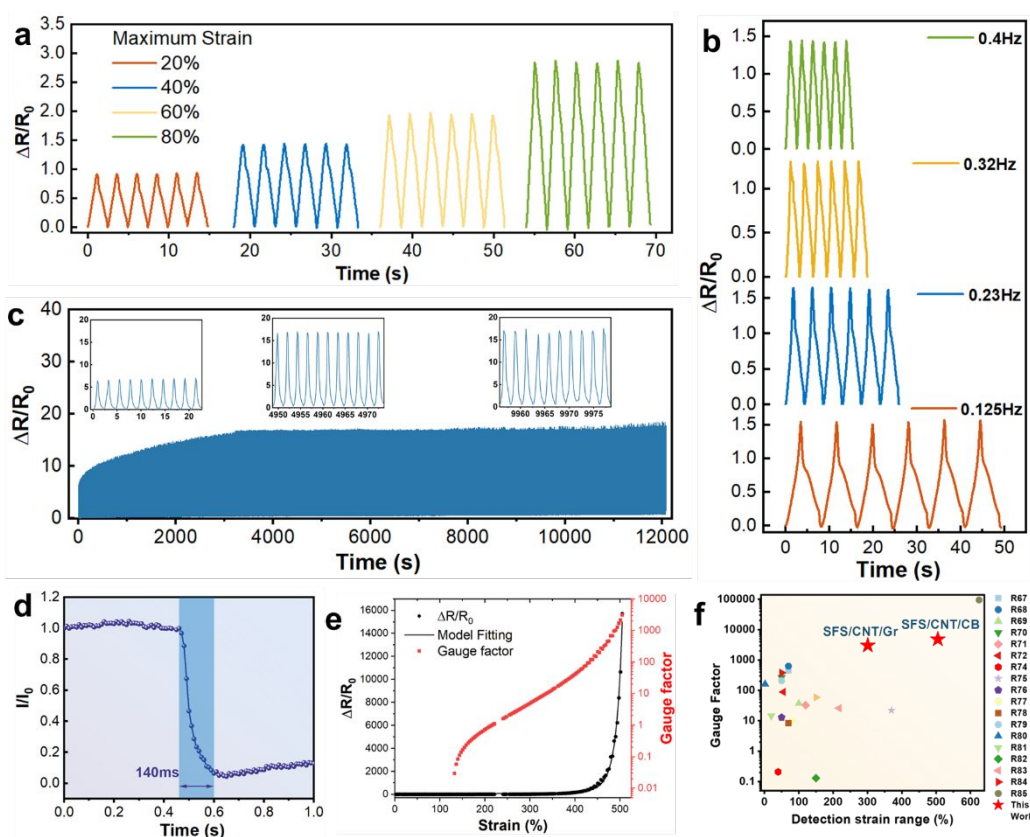mechanical deformation rate at all frequencies.

Figure 6. (a) The relative resistance change ($\Delta R/R_0$) of SFS/CNT/CB (90/3/7) nanocomposites under
cyclic stretching at different maximum strains under a frequency of 0.4Hz. (b) The relative resistance
change ($\Delta R/R_0$) of SFS/CNT/CB (90/3/7) under cyclic stretching at different frequencies with a
maximum strain of 40%. (c) The cycling stability of SFS/CNT/CB (90/3/7) under 100% maximum
strain with a duration of over 12000 seconds. (d) Electrical response time of SFS/CNT/CB (90/3/7)
during a rapid deformation. (e) The relative resistance change ($\Delta R/R_0$) and gauge factor as a function
of strain for SFS/CNT/CB (90/3/7) with a maximum strain of 500%. The solid line is fitting of $\Delta R/R_0$
by the analytical model. (f) Comparison of the gauge factors of our SFS/CNT/CB and SFS/CNT/Gr
composites with those of recently reported strain sensors.

The long-term response stability of SFS nanocomposites against mechanical deformation (0.45 Hz, maximum strain of 100%) is also studied (Figure 6c). It can be seen that the sensitivity or magnitude of the electrical response of SFS/CNT/CB (90/3/7) nanocomposite has a gradual increase up to 3000s. Then the response is highly stable and consistent across tens of thousands of cycles. The response rate of SFS/CNT/CB (90/3/7) nanocomposite is also tested with a fast deformation test as shown in Figure 6d. It only takes 140 ms for the composite to respond and complete the significant resistance change.

The relative resistance change across a large strain range (up to 500%) is shown in Figure 6e, it can be seen that when the strain reaches large values, there is an almost exponential increase in the resistance change with strain. For instance, the value of $\Delta R/R_0$ is about 15 at 300% strain, which rapidly increases to 200 at 400% strain, and over 10,000 at 500% strain. We also used analytical modeling based on Simmons approximation theory to fit the relationship between relative resistance change and mechanical strain[61]. In our case,

$$\left(\frac{\Delta R}{R_0}\right) = \frac{R - R_0}{R_0} = (1 + E\varepsilon)\exp((A + FE)\varepsilon + B\varepsilon^2 + C\varepsilon^3 + D\varepsilon^4) - 1 \cdots\cdots\cdots\cdots (1)$$

where *A, B, C,* and *D* are material system dependent constants, and they represent the non-linear change in the number of conductive pathways at large strains. *E* is another material system dependent constant that describes the change in the average spacing between neighboring conductive nanoparticles as a function of the applied strain. *F* is a parameter that depends on the potential barrier between conductive nanoparticles. Detailed derivation and explanation of the model can be found in the supporting information. The model fitting matches very well with the experimental data.

Gauge factor $\left(\frac{\Delta R}{R_0}/\varepsilon\right)$ is frequently used to assess the performance of strain sensors, and is also shown in Figure 6e (red curve with log scale). The SFS/CNT/CB (90/3/7) nanocomposite shows very large and fast-increasing gauge factors at strain above 200%. A similar trend of gauge factor is also obtained for SFS/CNT/Gr nanocomposites (Figure S6). The performance of our SFS nanocomposites as strain sensors is compared with recent literature reports with similar material systems (Figure 6f, see also Table S1)[67–85]. It can be seen that our SFS nanocomposites have excellent performance in terms of both large detection range of strain and high guage factor at large strains.

3.7 Demonstration of wearable sensors and environment monitoring

The combination of high elasticity, low modulus, chemical stability, tunable conductivity, and rapid strain response of SFS nanocomposites enables their promising application in stretchable and wearable sensors. We demonstrate this by using SFS/CNT/CB (90/3/7) nanocomposite as sensors for human motion detection. The detection of repeated elbow flexion is shown in Figure 7a. Mouth movement and closing are also accurately monitored (Figure 7b),

which can potentially be used for intelligent voice control. Subtle human motion such as rhythmic abdominal movement during breathing and finger bending detection are also demonstrated (Figure S13), which is applicable to soft robotics.
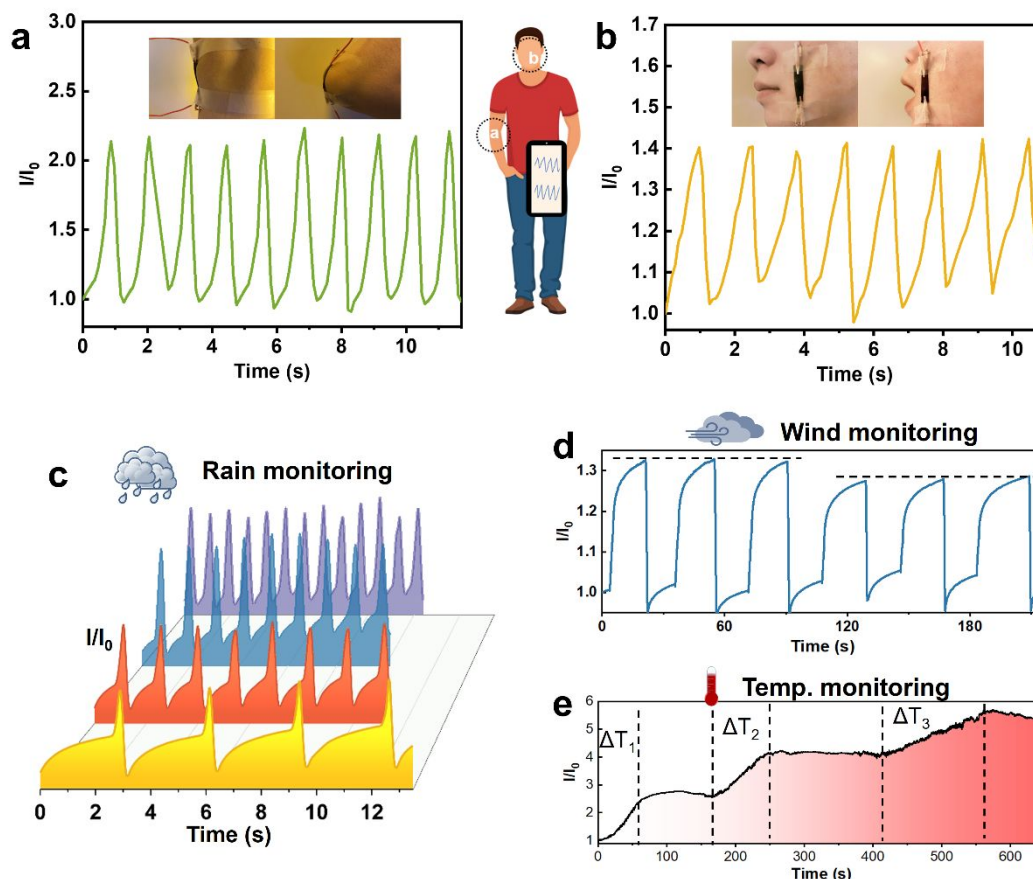
Figure 7. Demonstration of the use of SFS/CNT/CB (90/3/7) nanocomposites in human motion monitoring and simulated weather monitoring. (a) Elbow flexion detection. (b) Mouth movement detection. (c) Monitoring of simulated raindrops with varying frequencies. (d) Monitoring of simulated wind blowing with two different speeds. (e) Monitoring of environmental temperature changes with three different heating and equilibrium stages.

Moreover, we also demonstrate that SFS/CNT/CB (90/3/7) nanocomposite can be used for accurate monitoring of environmental conditions including rain, wind, or temperature changes. For instance, we used water drops falling on the soft sensor to simulate rain detection, with the mass of each droplet being about 40 mg and a speed of 4.5 m/s (from 1 meter height). Figure 7c shows the electrical current response of such simulated rainfall with different frequencies. The nanocomposite can also be used to detect wind (Figure 7d). The wind strokes that blow on the sample during the first 80 seconds have a speed of 17.0 m/s, and the subsequent wind strokes have a speed of 9.2 m/s. It can be seen that the magnitude of the current response is different at those two different wind speeds.

Last but not least, we demonstrate temperature monitoring by the SFS/CNT/CB (90/3/7)

nanocomposite. Sensitive responses to multiple heating stages and temperatures can be obtained (Figure 7e). For instance, in the first stage, the temperature increases from 20 °C to 44 °C, and then maintains stable for 100 s; in the second stage, the temperature further increases to 67 °C and remains stable for another 150 s; in the third stage, the temperature increases to 86 °C and then remain stable. The electrical current increases during each heating step and maintains stability when the temperature reaches equilibrium. The probable reason for the temperature-induced conductivity change is that the conductivity of CNTs increases with temperature due to the thermally activated process and increased charge carrier density[86,87]. As a result, our SFS/CNT/CB nanocomposites also show higher electrical conductivity at higher temperatures.

4. Conclusions

In summary, we developed a series of sustainable and 3D-printable soft nanocomposites by integrating SFS TPE and carbon nanomaterials. Due to the excellent mechanical properties, chemical stability, and processability of SFS, such nanocomposites are flexible and stretchable (> 1500%), with highly tunable internal structures and electrical properties, which are distinct from conventional soft composites with petrochemical-based soft matrix and a single type of nanofiller. Pellet 3D printing is also used as a new and efficient approach for fabricating customizable 3D structures and devices based on the SFS nanocomposites. The electrical responses of such SFS nanocomposites to mechanical deformation are highly tunable and diverse. Several key factors that determine such electrical responses including the type/geometry of carbon nanofillers, nanofiller loading, the ratio between the nanofillers, as well as the processing condition (3D printing vs solution casting) were systematically investigated. Our SFS nanocomposites have superior performance as strain sensors in terms of the maximum strain range and gauge factor at large strains. We also demonstrate the application of such SFS nanocomposites in human motion detection as well as environment monitoring. The sustainable and 3D-printable SFS nanocomposites provide a material platform for future research in soft sensors, wearable electronics, and soft robotics.

Data availability
The data supporting this article have been included as part of the Supplementary Information.

Author Contributions
W.X. designed and supervised the research. X.L. conducted most of the experiments and data analysis. N.S., J.B., M.Y., and X.G. contributed to the experiments. X.L. and W.X wrote the original manuscript. All authors reviewed and approved the final manuscript.

Conflicts of interest

The authors declare no conflict of interest.

ACKNOWLEDGMENTS

REFERENCES

1 T. Y. Kim, S. H. Hong, S. H. Jeong, H. Bae, S. Cheong, H. Choi and S. K. Hahn, *Advanced Materials*, 2023, **35**, 2303401.

2 J. Gao, Y. Fan, Q. Zhang, L. Luo, X. Hu, Y. Li, J. Song, H. Jiang, X. Gao, L. Zheng, W. Zhao, Z. Wang, W. Ai, Y. Wei, Q. Lu, M. Xu, Y. Wang, W. Song, X. Wang and W. Huang, *Advanced Materials*, 2022, **34**, 2107511.

3 C. Wang, D. Hwang, Z. Yu, K. Takei, J. Park, T. Chen, B. Ma and A. Javey, *Nature Mater*, 2013, **12**, 899–904.

4 L. Duan, D. R. D'hooge and L. Cardon, *Progress in Materials Science*, 2020, **114**, 100617.

5 D. C. Kim, H. J. Shim, W. Lee, J. H. Koo and D. Kim, *Advanced Materials*, 2020, **32**, 1902743.

6 K. Sim, Z. Rao, F. Ershad and C. Yu, *Advanced Materials*, 2020, **32**, 1902417.

7 Y. He, D. Wu, M. Zhou, Y. Zheng, T. Wang, C. Lu, L. Zhang, H. Liu and C. Liu, *ACS Appl. Mater. Interfaces*, 2021, **13**, 15572–15583.

8 S. J. Paul, I. Elizabeth and B. K. Gupta, *ACS Appl. Mater. Interfaces*, 2021, **13**, 8871–8879.

9 Y. Jia, X. Yue, Y. Wang, C. Yan, G. Zheng, K. Dai, C. Liu and C. Shen, *Composites Part B: Engineering*, 2020, **183**, 107696.

10 M. Fan, L. Wu, Y. Hu, M. Qu, S. Yang, P. Tang, L. Pan, H. Wang and Y. Bin, *Adv Compos Hybrid Mater*, 2021, **4**, 1039–1047.

11 S. C. B. Mannsfeld, B. C.-K. Tee, R. M. Stoltenberg, C. V. H.-H. Chen, S. Barman, B. V. O. Muir, A. N. Sokolov, C. Reese and Z. Bao, *Nature Mater*, 2010, **9**, 859–864.

12 W. Yang, J.-J. Liu, L.-L. Wang, W. Wang, A. C. Y. Yuen, S. Peng, B. Yu, H.-D. Lu, G. H. Yeoh and C.-H. Wang, *Composites Part B: Engineering*, 2020, **188**, 107875.

13 G. Georgousis, K. Roumpos, E. Kontou, A. Kyritsis, P. Pissis, S. Koutsoumpis, M. Mičušík and M. Omastová, *Composites Part B: Engineering*, 2017, **131**, 50–61.

14 Y.-R. Ding, C.-H. Xue, X.-J. Guo, X. Wang, S.-T. Jia and Q.-F. An, *Chemical Engineering Journal*, 2021, **409**, 128199.

15 H. Zhang, N. He, B. Wang, B. Ding, B. Jiang, D. Tang and L. Li, *Advanced Materials*, 2023, **35**, 2300398.

16 J. Chen, L. Zhang, Y. Tu, Q. Zhang, F. Peng, W. Zeng, M. Zhang and X. Tao, *Nano Energy*, 2021, **88**, 106272.

17 D. Xiang, X. Zhang, E. Harkin-Jones, W. Zhu, Z. Zhou, Y. Shen, Y. Li, C. Zhao and P. Wang, *Composites Part A: Applied Science and Manufacturing*, 2020, **129**, 105730.

18 Q. Zou, K. He, J. Ou-Yang, Y. Zhang, Y. Shen and C. Jin, *ACS Appl. Mater. Interfaces*, 2021, **13**, 14479–14488.

19 S. Liu, Y. Wu, L. Jiang, W. Xie, B. Davis, M. Wang, L. Zhang, Y. Liu, S. Xing, M. D. Dickey and W. Bai, *ACS Appl. Mater. Interfaces*, 2024, **16**, 46538–46547.

20 S. Mousavi, D. Howard, F. Zhang, J. Leng and C. H. Wang, *ACS Appl. Mater. Interfaces*, 2020, **12**, 15631–15643.

21 T. Xiao, C. Qian, R. Yin, K. Wang, Y. Gao and F. Xuan, *Adv Materials Technologies*, 2021, **6**, 2000745.

22 Y. He, M. Zhou, M. H. H. Mahmoud, X. Lu, G. He, L. Zhang, M. Huang, A. Y. Elnaggar, Q. Lei, H. Liu, C. Liu and I. H. E. Azab, *Adv Compos Hybrid Mater*, 2022, **5**, 1939–1950.

23 X. Zhang, L. Ke, X. Zhang, F. Xu, Y. Hu, H. Lin and J. Zhu, *ACS Appl. Mater. Interfaces*, 2022, **14**, 25753–25762.

24 L. Zhou, J. Fu, Q. Gao, P. Zhao and Y. He, *Adv Funct Materials*, 2020, **30**, 1906683.

25 S. Tang, J. Li, R. Wang, J. Zhang, Y. Lu, G. Hu, Z. Wang and L. Zhang, *SusMat*, 2022, **2**, 2–33.

26 D. Jung, C. Lim, C. Park, Y. Kim, M. Kim, S. Lee, H. Lee, J. H. Kim, T. Hyeon and D. Kim, *Advanced Materials*, 2022, **34**, 2200980.

27 R. Bonart, *Polymer*, 1979, **20**, 1389–1403.

28 R. J. Spontak and N. P. Patel, *Current Opinion in Colloid & Interface Science*, 2000, **5**, 333–340.

29 M. Steube, T. Johann, R. D. Barent, A. H. E. Müller and H. Frey, *Progress in Polymer Science*, 2022, **124**, 101488.

30 P. Sahu, J. Young Ko, J. Uk Ha and J. S. Oh, *Ind. Eng. Chem. Res.*, 2023, **62**, 8726–8735.

31 C. Wahlen and H. Frey, *Macromolecules*, 2021, **54**, 7323–7336.

32 P. B. V. Scholten, C. Detrembleur and M. A. R. Meier, *ACS Sustainable Chem. Eng.*, 2019, **7**, 2751–2762.

33 K. R. Benjamin, I. R. Silva, J. P. Cherubim, D. McPhee and C. J. Paddon, *Journal of the Brazilian Chemical Society*, DOI:10.5935/0103-5053.20160119.

34 United States, US20160108228A1, 2016.

35 United States, US7759444B1, 2010.

36 D. H. Lamparelli, V. Paradiso, F. D. Monica, A. Proto, S. Guerra, L. Giannini and C. Capacchione, *Macromolecules*, 2020, **53**, 1665–1673.

37 P. Sahu and J. S. Oh, *Ind. Eng. Chem. Res.*, 2022, **61**, 11815–11824.

38 P. Martins, N. Pereira, A. C. Lima, A. Garcia, C. Mendes-Filipe, R. Policia, V. Correia and S. Lanceros-Mendez, *Adv Funct Materials*, 2023, **33**, 2213744.

39 N. Shen, J. Bu, M. E. Prévôt, T. Hegmann, J. P. Kennedy and W. Xu, *Macromol. Rapid Commun.*, 2023, **44**, 2200109.

40 M. Yang, J. Bu, N. Shen, S. Liu and W. Xu, *Adv Materials Technologies*, 2025, **10**, 2400890.

41 S. Liu, M. Yang, C. Smarr, G. Zhang, H. Barton and W. Xu, *ACS Appl. Bio Mater.*, 2024, **7**, 3247–3257.

42 B. Duncan, D. Beck, P. Miller, R. Benz, K. Ledford, A. Rosh-Gorsky and M. Smith, *ACS Materials Lett.*, 2024, **6**, 720–728.

43 Z. Jiang, O. Erol, D. Chatterjee, W. Xu, N. Hibino, L. H. Romer, S. H. Kang and D. H. Gracias, *ACS Appl. Mater. Interfaces*, 2019, **11**, 28289–28295.

44 N. Shen, L. Duan, M. Yang, S. Liu and W. Xu, *MRS Communications*, 2022, **12**, 597–602.

45 S. Park, W. Shou, L. Makatura, W. Matusik and K. (Kelvin) Fu, *Matter*, 2022, **5**, 43–76.

46 D. G. Bekas, Y. Hou, Y. Liu and A. Panesar, *Composites Part B: Engineering*, 2019, **179**, 107540.

47 W. Xu, S. Jambhulkar, Y. Zhu, D. Ravichandran, M. Kakarla, B. Vernon, D. G. Lott, J. L. Cornella, O. Shefi, G. Miquelard-Garnier, Y. Yang and K. Song, *Composites Part B: Engineering*, 2021, **223**, 109102.

48 M. Zhou, J. Li, P. Reyes, M. Erkoç, G. Wang, M. Edeleva, N. Zhu, M. Deng, L. Cardon and D. R. D'hooge, *Nano Energy*, 2025, **135**, 110629.

49 A. Osman and J. Lu, *Materials Science and Engineering: R: Reports*, 2023, **154**, 100734.

50 N. Shen, S. Liu, P. Kasbe, F. Khabaz, J. P. Kennedy and W. Xu, *ACS Appl. Polym. Mater.*, 2021, **3**, 4554–4562.

51 J. Bu, N. Shen, Z. Qin and W. Xu, *Cell Reports Physical Science*, 2023, **4**, 101604.

52 B. Duncan, R. D. Weeks, B. Barclay, D. Beck, P. Bluem, R. Rojas, M. Plaut, J. Russo, S. G. M. Uzel, J. A. Lewis and T. Fedynyshyn, *Adv Materials Technologies*, 2023, **8**, 2201496.

53 N. Zhou, Y. Bekenstein, C. N. Eisler, D. Zhang, A. M. Schwartzberg, P. Yang, A. P. Alivisatos and J. A. Lewis, *Science Advances*, 2019, **5**, eaav8141.

54 M. Kim, S. Nian, D. A. Rau, B. Huang, J. Zhu, G. Freychet, M. Zhernenkov and L.-H. Cai, *ACS Polym. Au*, 2024, **4**, 98–108.

55 B. B. Patel, D. J. Walsh, D. H. Kim, J. Kwok, B. Lee, D. Guironnet and Y. Diao, *Sci. Adv.*, 2020, **6**, eaaz7202.

56 F. Pignatelli and G. Percoco, *Prog Addit Manuf*, 2022, **7**, 1363–1377.

57 A. La Gala, R. Fiorio, M. Erkoç, L. Cardon and D. R. D'hooge, *Processes*, 2020, **8**, 1522.

58 D. V. A. Ceretti, M. Edeleva, L. Cardon and D. R. D'hooge, *Molecules*, 2023, **28**, 2344.

59 M. Zhou, P. J. González, L. Van Haasterecht, A. Soylu, M. Mihailovski, P. Van Zuijlen and M. L. Groot, *Biomech Model Mechanobiol*, 2024, **23**, 911–925.

60 N. S. Karode, A. Poudel, L. Fitzhenry, S. Matthews, P. R. Walsh and A. B. Coffey, *Polymer Testing*, 2017, **62**, 268–277.

61 D. Xiang, X. Zhang, Y. Li, E. Harkin-Jones, Y. Zheng, L. Wang, C. Zhao and P. Wang, *Composites Part B: Engineering*, 2019, **176**, 107250.

62 S. Yu, X. Wang, H. Xiang, L. Zhu, M. Tebyetekerwa and M. Zhu, *Carbon*, 2018, **140**, 1–9.

63 P. Xu, S. Wang, A. Lin, H.-K. Min, Z. Zhou, W. Dou, Y. Sun, X. Huang, H. Tran and X. Liu, *Nat Commun*, 2023, **14**, 623.

64 J. M. Clough, C. Creton, S. L. Craig and R. P. Sijbesma, *Adv Funct Materials*, 2016, **26**, 9063–9074.

65 T. Schmaltz, L. Wormer, U. Schmoch and H. Döscher, *2D Mater.*, 2024, **11**, 022002.

66 F. Orozco, A. Salvatore, A. Sakulmankongsuk, D. R. Gomes, Y. Pei, E. Araya-Hermosilla, A. Pucci, I. Moreno-Villoslada, F. Picchioni and R. K. Bose, *Polymer*, 2022, **260**, 125365.

67 Y. Hu, T. Huang, H. Lin, L. Ke, W. Cao, C. Chen, W. Wang, K. Rui and J. Zhu, *J. Mater. Chem. A*, 2022, **10**, 928–938.

68 Q. Duan, B. Lan and Y. Lv, *ACS Appl. Mater. Interfaces*, 2022, **14**, 1973–1982.

69 S. Zhu, H. Sun, Y. Lu, S. Wang, Y. Yue, X. Xu, C. Mei, H. Xiao, Q. Fu and J. Han, *ACS Appl. Mater. Interfaces*, 2021, **13**, 59142–59153.

70 X.-C. Tan, J.-D. Xu, J.-M. Jian, G.-H. Dun, T.-R. Cui, Y. Yang and T.-L. Ren, *ACS Nano*, 2021, **15**, 20590–20599.

71 S. Wu, S. Peng, Z. J. Han, H. Zhu and C. H. Wang, *ACS Appl. Mater. Interfaces*, 2018, **10**, 36312–36322.

72 G. Li, K. Dai, M. Ren, Y. Wang, G. Zheng, C. Liu and C. Shen, *J. Mater. Chem. C*, 2018, **6**, 6575–

6583.

73 Y. Jiang, Y. Chen, W. Wang and D. Yu, *Colloids and Surfaces A: Physicochemical and Engineering Aspects*, 2021, **629**, 127477.

74 A. Shaker, A. H. Hassanin, N. M. Shaalan, M. A. Hassan and A. A. El-Moneim, *Smart Mater. Struct.*, 2019, **28**, 075029.

75 Y. Wang, W. Li, Y. Zhou, L. Jiang, J. Ma, S. Chen, S. Jerrams and F. Zhou, *J Mater Sci*, 2020, **55**, 12592–12606.

76 L. Lu, X. Wei, Y. Zhang, G. Zheng, K. Dai, C. Liu and C. Shen, *J. Mater. Chem. C*, 2017, **5**, 7035–7042.

77 Z. Jia, Z. Li, S. Ma, W. Zhang, Y. Chen, Y. Luo, D. Jia, B. Zhong, J. M. Razal, X. Wang and L. Kong, *Journal of Colloid and Interface Science*, 2021, **584**, 1–10.

78 Q. Xia, S. Wang, W. Zhai, C. Shao, L. Xu, D. Yan, N. Yang, K. Dai, C. Liu and C. Shen, *Composites Communications*, 2021, **26**, 100809.

79 Y. Wang, F. Wang, S. Yazigi, D. Zhang, X. Gui, Y. Qi, J. Zhong and L. Sun, *Carbon*, 2021, **173**, 849–856.

80 Z. Liu, D. Qi, P. Guo, Y. Liu, B. Zhu, H. Yang, Y. Liu, B. Li, C. Zhang, J. Yu, B. Liedberg and X. Chen, *Advanced Materials*, 2015, **27**, 6230–6237.

81 N. Qaiser, F. Al-Modaf, S. M. Khan, S. F. Shaikh, N. El-Atab and M. M. Hussain, *Adv Funct Materials*, 2021, **31**, 2103375.

82 F. Zhang, D. Ren, L. Huang, Y. Zhang, Y. Sun, D. Liu, Q. Zhang, W. Feng and Q. Zheng, *Adv Funct Materials*, 2021, **31**, 2107082.

83 M. Lin, Z. Zheng, L. Yang, M. Luo, L. Fu, B. Lin and C. Xu, *Advanced Materials*, 2022, **34**, 2107309.

84 F. Zhang, L. Guo, Y. Shi, Z. Jin, Y. Cheng, Z. Zhang, C. Li, Y. Zhang, C. H. Wang, W. Feng and Q. Zheng, *Chemical Engineering Journal*, 2023, **452**, 139664.

85 L. Duan, M. Spoerk, T. Wieme, P. Cornillie, H. Xia, J. Zhang, L. Cardon and D. R. D'hooge, *Composites Science and Technology*, 2019, **171**, 78–85.

86 S. Fujita and A. Suzuki, *Journal of Applied Physics*, 2010, **107**, 013711.

87 M. Mohiuddin and S. V. Hoa, *Composites Science and Technology*, 2011, **72**, 21–27.

Data availability

The data supporting this article have been included as part of the Supplementary Information.